Structure and motion of edge turbulence in the National Spherical Torus Experiment and Alcator C-Mod[a)]

S. J. Zweben[b)]
Princeton Plasma Physics Laboratory, Princeton, New Jersey 08540

R. J. Maqueda
Nova Photonics, Princeton, New Jersey 08540

J. L. Terry
MIT, Cambridge, Massachusetts 02139

T. Munsat
Univ. Colorado, Boulder, Colorado 80309

J. R. Myra, D. D'Ippolito, and D. A. Russell
Lodestar Research, Boulder, Colorado 80301

J. A. Krommes, B. LeBlanc, T. Stoltzfus-Dueck, D. P. Stotler, and K. M. Williams
Princeton Plasma Physics Laboratory, Princeton, New Jersey 08540

C. E. Bush and R. Maingi
ORNL, Oak Ridge, Tennessee 37831

O. Grulke
MPI for Plasma Physics, Euratom Association. Greifswald, Germany

S. A. Sabbagh
Columbia University, New York, New York 10027

A. E. White
UCLA, Los Angeles, Calilfornia 90095

(Received 28 October 2005; accepted 20 January 2005; published online 15 May 2006)

In this paper we compare the structure and motion of edge turbulence observed in L-mode vs. H-mode plasmas in the National Spherical Torus Experiment (NSTX) [M. Ono, M. G. Bell, R. E. Bell *et al.*, Plasma Phys. Controlled Fusion **45**, A335 (2003)]. The radial and poloidal correlation lengths are not significantly different between the L-mode and the H-mode in the cases examined. The poloidal velocity fluctuations are lower and the radial profiles of the poloidal turbulence velocity are somewhat flatter in the H-mode compared with the L-mode plasmas. These results are compared with similar measurements Alcator C-Mod [E. Marmar, B. Bai, R. L. Boivin *et al.*, Nucl. Fusion **43**, 1610 (2003)], and with theoretical models. © *2006 American Institute of Physics*. [DOI: 10.1063/1.2177132]

I. INTRODUCTION

Edge turbulence has been measured for many years in tokamaks and other toroidal magnetic fusion devices, most recently using two-dimensional (2-D) diagnostic techniques.[1–3] The results have been fairly consistent over a wide variety of devices; namely, that the edge is strongly unstable in the "drift wave" range of size scales (~0.1 to 10 cm) and frequencies (~10 kHz to 1000 kHz), with typical density fluctuation levels $\tilde{n}/n \sim 5-50\%$ near the last closed magnetic flux surface, at least at the outboard midplane. This edge turbulence is important since it dominates radial transport in the scrape-off layer, which can affect the plasma-wall interaction, and since it probably determines the H-mode threshold, which can affect the global plasma confinement.

Despite a wealth of experimental data there is so far little direct comparison of these edge turbulence measurements with first-principles turbulence models or simulations. However, these models have been evolving rapidly,[4–8] so direct comparisons are becoming more feasible. In this paper we present recent edge turbulence imaging data from NSTX (National Spherical Torus Experiment) and briefly compare the results to Alcator C-Mod and to some recent theoretical models.

Section II describes the edge turbulence diagnostic used for these measurements, and Sec. III describes the recent NSTX results. The discussion of Sec. IV contains a comparison between NSTX and the Alcator C-Mod, a comparison with previous results experimental and theoretical models, directions for future work, and a conclusion.

II. GAS PUFF IMAGING DIAGNOSTIC

The gas puff imaging (GPI) diagnostic used for these turbulence imaging measurements has been described

[a)]Paper CI1b 1, Bull. Am. Phys. Soc. **50**, 63 (2005).
[b)]Invited speaker.

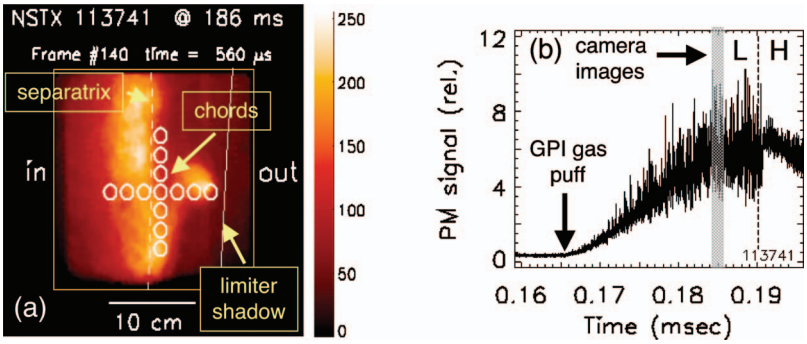

FIG. 1. (Color) Part (a) shows a single frame from a sequence of 300 images captured by the fast camera during an NSTX discharge. The 64×64 pixel frame shows the GPI light emission in D_α for a region 23 cm poloidally (up/down) by 23 cm radially (left/right) with an exposure time of 4 μs. The locations of the radial and poloidal chord arrays are superimposed on the image, along with the locations of the EFIT magnetic separatrix, the outer limiter shadow, and the color scale. In part (b) is a typical time dependence of the GPI light emission as digitized from one chord, showing the rise of the signal with the GPI gas puff at 0.165 s and an L-H transition at 0.19 s.

previously.[9–12] For the present paper the visible D_α (656 nm) line emission from a deuterium gas puff was used to image the turbulent fluctuations. Since the turbulence is highly elongated along the total magnetic field B, the visible light from the gas puff cloud was viewed along the local B field in the cloud to within a few degrees to resolve the radial and poloidal structure of the turbulence. The gas cloud increases the brightness of the emission and localizes it along this viewing line for improved spatial resolution.

Some hardware improvements were made to the present GPI diagnostic compared to that described previously. First, an 8×10 mm coherent fiber optic bundle was used instead of a 4×4 mm bundle, which increased the signal level by about a factor of 5. Second, the gas puff manifold was moved closer to the plasma edge to decrease the toroidal extent of the gas cloud in order to improve the spatial resolution, which is now about 1–2 cm. Third, a new Princeton Scientific Instruments PSI-5 camera was used; this camera can store 300 frames with spatial resolution of 64 pixels (poloidally) $\times64$ pixels (radially), compared with 28 frames for the previous PSI-4 camera.[9] At the normal frame rate of 250 000 frames/s the PSI-5 camera captures 1.2 ms of data for each NSTX shot.

Figure 1(a) shows a typical image of a single frame from the PSI-5 camera. The field of view at the plasma is 23 cm radially by 23 cm poloidally, centered radially near the magnetic separatrix, and about 20 cm poloidally above the outer midplane of NSTX ($R=85$ cm, $a=65$ cm). The orientation of the bundle is arranged so that the local radial direction is horizontal (outward to the right) and the local poloidal direction (within a magnetic flux surface) is vertical, with the ion diamagnetic and grad-B drift direction down. Superimposed on this image are the locations of 13 discrete "chords," each of which was fiberoptically coupled to a photomultiplier tube and digitized at 500 kHz for 64 ms. At the GPI gas cloud the chord centers were separated by 2 cm and viewed a diameter of 2 cm. A typical signal versus time from one of these chords is shown in Fig. 1(b). The analog bandwidth of these chord signals was $\approx$200 kHz.

The interpretation of the GPI images has already been described.[9–12] The light emission in the D_α line is located in the region where the neutrals are significantly excited but not yet ionized, which corresponds roughly to $T_e\approx5-100$ eV. Within this temperature range, which is roughly ±5 cm around the separatrix in NSTX, the line emission at a given neutral density is a nonlinear (but monotonically increasing) function of the local electron density n_e and electron temperature T_e.[13] However, as discussed in Ref. 9, the structure and motion of the GPI light fluctuations, as defined by the space-time cross-correlation functions, is approximately independent of the details of this nonlinearity. This effect is similar to a TV image in which the structure and motion is roughly independent of the nonlinearity controlled by the contrast setting. For the camera images in this paper, there was an additional nonlinearity due to the microchannel plate of the PSI-5 camera, for which the output signal level was roughly proportional to the square root of the light intensity over this range of intensities. This nonlinearity had no effect on the chord signals.

III. NSTX RESULTS

A. Plasma parameters

Most of the results described in this paper were obtained for a set of about 20 discharges taken on a single run day with plasma parameters shown in Table I (#113732-113750). These discharges had a relatively small toroidal field ($B_0=3$ kG) and a modest amount of NBI power (2–4 MW); nevertheless, their qualitative behavior was similar to other NBI-heated L-mode and H-mode discharges in NSTX.[9] All these discharges had transitions from the L- (low confinement) mode to the H- (high confinement) mode, which were captured in either the camera data or the chord data, or both.

TABLE I. NSTX parameters.

$R=0.85$ m
$a=0.68$ m
$B_0=3$ kG
$I_p=0.8$ MA
$P_{NBI}=2$–4 MW
$T_e(0)=0.5$–1 keV
$n_e(0)=2\text{-}4\times10^{13}$ cm^{-3}
$\tau_E\approx30$ ms
$\beta_{tor}\approx10\%$
$n_e(\text{edge})\approx0.2$–$2\times10^{13}$ cm^{-3}
$T_e(\text{edge})=5$–50 eV
$L_\perp\sim2$–5 cm
$L_{II}\sim5$ m
$\rho_s\sim0.2$ cm
$\beta_e\sim10^{-3}$

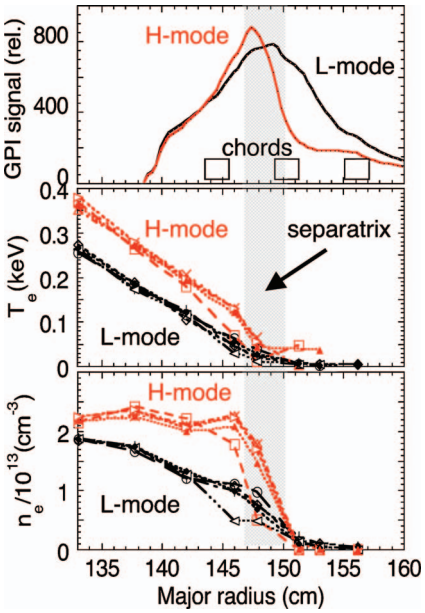

FIG. 2. (Color) Radial profiles of the GPI light emission and Thomson scattering measurements for the edge plasmas used for this paper. The GPI signal profiles are the time averages over the L-mode and H-mode periods, as measured by the camera. The locations of the center, innermost, and outermost radial chords are shown at the top. The GPI light emission region has a radial width of $\approx \pm 10$ cm around the magnetic separatrix (as inferred from EFIT). The Thomson scattering profiles with an L-mode in black and an H-mode in red, were taken within ±8 ms of the L-H transition for four similar shots. The GPI light emission during H-mode peaks within the high density gradient region of the pedestal.

Shots #113732-45 had a near-double-null configuration; shots #113747-50 had the same plasma parameters, but with a lower-single null.

Figure 2 shows the edge plasma profiles for the discharges described in this paper. The radial coordinate is the major radius at the outer midplane. The GPI signal intensity profiles come from the time-averaged camera images as mapped along a flux surface to the outer midplane, and span a radial region of about ±10 cm around the magnetic separatrix, as derived from EFIT.[14] The n_e and T_e profiles come from Thomson scattering for four similar shots in this sequence, all taken with ±8 ms with respect to the L-H transition. The formation of a pedestal in edge density and temperature just after the L-H transition can be seen, although the details of the profile shape are difficult to determine, given the relatively coarse space and time resolution of the Thomson scattering system. Note that the GPI light emission during H-mode peaks within the high-density gradient region of the pedestal.

B. Qualitative description of the data

An example of the image data from a shot with a L-H transition is shown in Fig. 3 (#113732). This mosaic shows 48 successive frames from a 300 frame movie, each of which was exposed for 4 μs with the field of view of Fig. 1. The only image analysis was "despeckling" with a 3×3 median filter, and only one common intensity normalization was used for all frames. Frames #130-153 were just before the L-H transition, frames #154-161 were during the transition, and frames #162-177 were after the transition. A movie of the image data from this and many similar shots can be seen at http://www.pppl.gov/~szweben/NSTX04/NSTX_04.html

The qualitative impression from the movie of this other similar data is that the L-mode turbulence consists of random fluctuations that are moving mostly downward, but sometimes upward, with occasional isolated "blobs" forming near the separatrix and moving radially outward. After the transition, the emission region narrowed and the fluctuation level was reduced [see Fig. 1(b)], with the remaining fluctuations

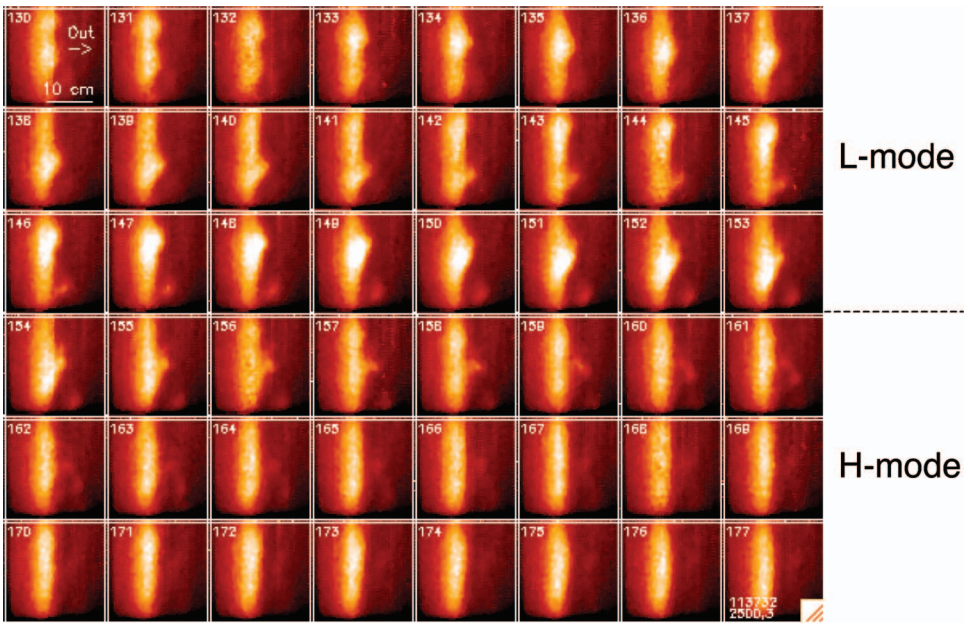

FIG. 3. (Color) An example of the image data from a shot with an L-H transition (#113732). This mosaic shows 48 successive frames from a 300 frame movie, each frame of which was exposed for 4 μs with the same field of view of as shown in Fig. 1(a). Frames #130-153 were just before the L-H transition, frames #154-161 were during the transition, and frames #162-177 were after the transition.

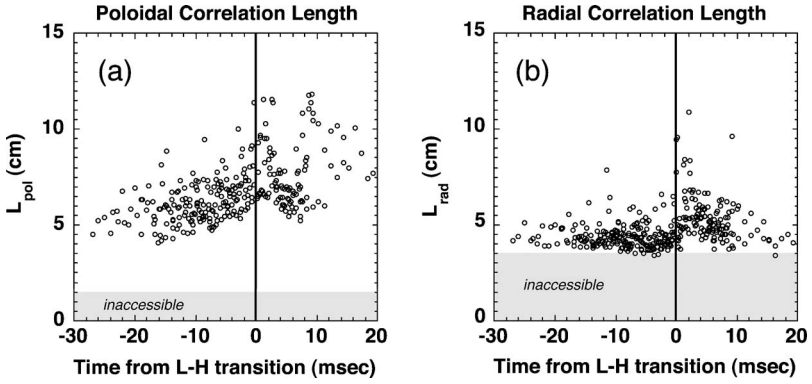

FIG. 4. Time dependence of the (a) poloidal and (b) radial correlation lengths as inferred from the chord data for a set of 13 consecutive discharges (#113732-113744) for times near the L-H transition. Each point represents the analysis of a 1 ms interval for one of these shots. The poloidal correlation length was $L_{pol} \approx 6.3 \pm 1.2$ cm before the transition and $L_{pol} \approx 7.5 \pm 2$ cm after the transition, and the radial correlation length was $L_{rad} \approx 4.3 \pm 0.8$ before the transition and $L_{rad} \approx 5.2 \pm 1.2$ after the transition (all FWHM). Thus there was no statistically significant difference in either L_{pol} or L_{rad} between the L-mode and the H-mode. The inaccessible regions due to the finite spacing of the chords are shown in gray.

moving more uniformly downward with less frequent blob generation. During the transition, the structures and motions seem to "morph" smoothly between these two conditions without the appearance of any new structure or motion. It looks as if the turbulence was just "turned off" with no obvious precursor or "trigger" for the L-to-H-mode transition, at least within this field of view. On the other hand, the few available images of H-mode to L-mode transitions show a local small-scale instability growing rapidly into blob-like radial motion within the GPI view.[15]

C. Spatial structure analysis

We define the cross-correlation function between two time series signals "S_0" and "$S_{\Delta x}$," which are separated by a distance "Δx" (radially or poloidally), and by an artificially introduced time delay "Δt," as

$$C(\Delta x, \Delta t) = \Sigma_t S_0(t) S_{\Delta x}(t + \Delta t) \quad (1)$$

where the sum is taken over the common time interval of both signals. The time-averaged value of both signals is removed before this calculation; thus this estimate is not affected by the spatial calibration, and just evaluates the degree of correlation between the temporal behavior at the two points. This cross-correlation function averages over the whole frequency and wave number spectrum.

For an estimate of the poloidal correlation length, the time delay was set to $\Delta t = 0$ and the value of C between the central chord and the other chords in the poloidal array (each separated by $\Delta x = 2$ cm) was plotted as a function of their separation. The poloidal correlation length L_{pol} was defined as the full width at half-maximum (FWHM) of this curve of C vs Δx (this FWHM is equivalent to ≈ 1.6 times the half-width of a Gaussian of the same shape). The raw data were smoothed by a median filter over 3×3 pixels (≈ 1 cm in space) before the analysis.

Figure 4(a) shows the time evolution of the poloidal correlation length before and after the L-H transition, as evaluated from the chord arrays for a set of 13 consecutive shots, such as described in Sec. III A. The horizontal axis is the time of the main (i.e., first) L-H transition, which varies from 0.183–0.202 s for these shots. Each point represents the correlation length estimated for a 1 ms time interval for that shot (i.e., 500 time points). The central chord in the array was located near the radial peak of the GPI light emission, as shown in Figs. 1 and 2. The result was that the poloidal correlation had an average value of $L_{pol} \approx 6.3 \pm 1.2$ cm before the transition, 7.5 ± 2 cm after the transition, and 6.8 ± 1.5 cm overall. There was a slow increase in L_{pol} over the 20 ms preceeding the transition, but little if any change in L_{pol} within ±5 ms of the transition. The second-to-bottom channel was not working properly for this data, so a linear interpolation was used instead of it. Correlation lengths below 2 cm were not accessible due to the finite spacing of these chords.

For the radial correlation length estimate in Fig. 4(b), the FWHM was determined by correlating the central radial chord with the two radial chords ±4 cm inside and outside of it (the two radial chords adjacent to the central chord were not working properly for these shots). The FWHM of this three-point cross-correlation function (linearly interpolated) is plotted in Fig. 4(b), with the result that $L_{rad} \approx 4.3 \pm 0.8$ cm before the L-H transition, 5.2 ± 1.2 cm after the transition, and 4.8 ± 1 cm overall. Since the spacing of these chords is comparable to the radial correlation length, some of these data points probably belong inside the "inaccessible region" below $L_{rad} \sim 4$ cm, so these average radial correlation lengths are somewhat overestimated. Nevertheless, it can be concluded that there was no significant reduction in the average radial correlation length from before to after the L-H transition in this dataset.

The structure of the turbulence was also obtained from the 2-D images in essentially the same way, i.e., from $C(\Delta x, 0)$, although these data were obtained for only 1.2 ms per shot (i.e., 300 frames at 250 000 frames/s). In these analyses the poloidal cross-correlation functions were centered at the up/down center of the images, and the radial cross-correlation functions were centered at the peak of the time-averaged emission profile to maximize the signal/noise ratio. The correlation analyses were done for each line or column within the range ±2 cm radially and ±5 cm poloidally around these centers. Note that for the H-mode cases this analysis was done in the high gradient region of the edge pedestal, as shown in Fig. 2. The raw data was smoothed by a median filter over 3×3 pixels before analysis.

Figure 5 shows the relationship between L_{pol} and L_{rad} derived from the 2-D images for 18 shots with the parameters in Table I. Each of the 11 L-mode points represents one shot of those used in Fig. 4, while the four H-mode points comes from other shots from the same day. The error bars on each point represent the standard deviation with the spatial

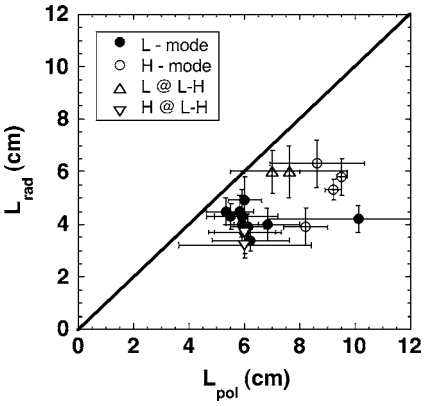

FIG. 5. Radial versus poloidal correlation lengths inferred from the camera images for a set of discharges of various types in this dataset. For the L-mode and H-mode cases, each point represents the analysis of one shot, with the result that for the L-mode, $L_{\mathrm{pol}} \approx 6.3 \pm 1.3$ and $L_{\mathrm{rad}} \approx 4.2 \pm 0.4$ cm, while for the H-mode $L_{\mathrm{pol}} \approx 8.9 \pm 1.6$ cm and $L_{\mathrm{rad}} \approx 5.3 \pm 1.0$ cm (all FWHM). For the L-H cases each point represents the analysis of the L-mode versus the H-mode phase of the same shot. The error bars represent the spatial variation over the regions of analysis. There were no statistically significant variations between L-mode and H-mode correlation lengths in this dataset.

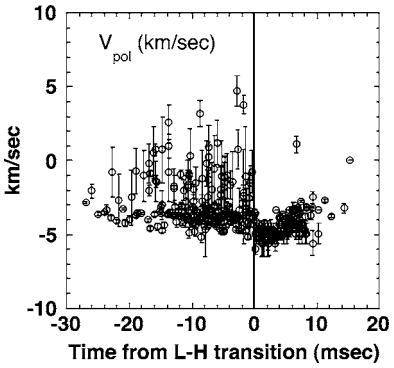

FIG. 6. Time dependence of the poloidal turbulence velocity as inferred from the poloidal array of chords for the same set of discharges as in Fig. 4. The error bars represent the standard deviation of the fits to the velocity profiles over 1 ms time intervals for each shot. At this radius there was a significant reduction in the fluctuations in the poloidal velocity just after the H-mode transition.

range of analysis for that shot. The average correlation lengths are similar to those shown in Fig. 5; namely, $L_{\mathrm{pol}} \pm 6.3 \pm 1.3$ cm and $L_{\mathrm{rad}} \pm 4.2 \pm 0.4$ cm for the L-mode, and $L_{\mathrm{pol}} \approx 8.9 \pm 1.6$ cm and $L_{\mathrm{rad}} \approx 5.3 \pm 1.0$ cm for the H-mode, where these error bars represent the shot-to-shot variations. The triangles show two shots in which the L-to-H transition was captured by the camera, for which the L-mode and H-mode periods of each were analyzed separately (#113732 and #113631). The results are similar to the other points, but perhaps there was a slight reduction in the radial correlation length just after the H-mode transition in these cases.

In summary, the result from Figs. 4 and 5 show no statistically significant change in either the poloidal or radial correlation lengths between the L-mode and H-mode in this dataset. Some uncertainties and limitations of these results are discussed in Sec. IV C.

D. Poloidal velocity analysis

Figure 6 shows the poloidal turbulence velocity obtained from the poloidal array of chords, as determined by the time delay of the peak of the cross-correlation functions between the central chord and all other poloidal chords [see Eq. (1)]. The poloidal velocity was derived from a linear fit to these time delays, and the error bars are the standard deviations of this fit. The same set of 13 consecutive shots of Fig. 4 was used, along with the same 1 ms time bins. The central chord was located near the time-averaged peak of the signals, which was slightly outside the separatrix. The second-to-bottom channel was not working properly for these data so a linear interpolation was used there.

The result of Fig. 6 is that the time-averaged poloidal velocity at this radius for this dataset increased from $V_{\mathrm{pol}} = -2.9 \pm 1.6$ km/s in the L-mode to -4.3 ± 1.2 km/s in the H-mode (the ion diamagnetic drift velocity direction is negative in this graph). A more significant change was that the fluctuations in poloidal velocity were reduced in the H-mode; for example, from -3.0 ± 3 km/s in 5 ms before the L-H transition, to -4.8 ± 0.49 km/s in the 5 ms just after the transition. Thus the poloidal motion appeared to be more "frozen" in the H-mode than in the L-mode.

Figure 7 shows the radial profiles of the poloidal turbulence velocity derived from images for four of the L-mode and four of the H-mode shots used in Fig. 5. Each point represents the poloidal velocity derived for one column of the image data for one shot, averaged over the time duration of the image. The radial coordinate is the distance from the EFIT separatrix for each shot, and all velocities are in the ion

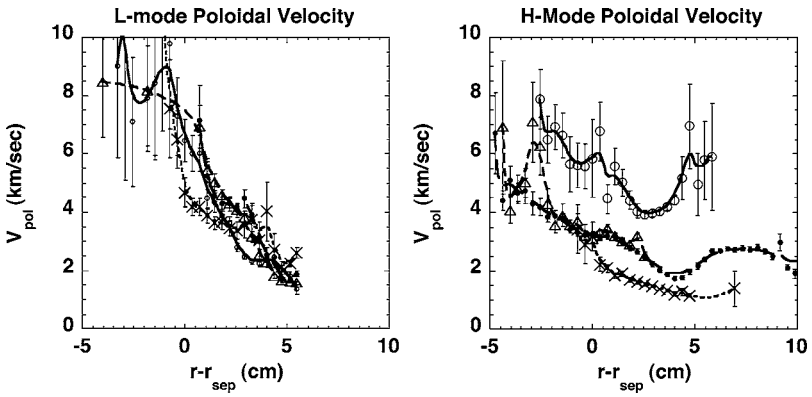

FIG. 7. Radial profiles of the poloidal turbulence velocity inferred from the camera images for four L-mode and four H-mode discharges. In the region near or just outside the separatrix the average radial gradient in the poloidal velocity is smaller in the H-mode than in the L-mode. The error bars represent the standard deviation of the velocity fit, averaged over the 1.2 ms. The variations in velocity are generally smaller in the H-mode than in the L-mode.

diamagnetic drift direction. The method for determining the velocity was the same as for Fig. 5, except that only points with $C(\Delta x, 0) \geqslant 0.5$ from the central (up/down centered) pixel in the image were used in the fitting process. One of the H-mode shots in Fig. 7 (with circled points, #113745) was similar to those used in Fig. 6, and showed a similar velocity at that radius ($\sim$5 km/s). The other three H-mode cases of Fig. 7 (#113747, #113748, #113759) had a lower single null instead of a near-double null as for the other shots, but still with the parameters shown in Table I. The latter three cases were taken at $\approx$100 ms after the L-H transition, while the first was taken at $\approx$20 ms after the L-H transition.

The general trend shown in Fig. 7 is for a lower average velocity gradient in the H-mode cases compared to the L-mode cases within this range of radii. For radial positions $(r-r_{sep}) \sim 0$ to 5 cm, the average radial gradient in the L-mode was roughly $\nabla V_{pol} \sim 1$ (km/s)/cm $\approx 10^5\ s^{-1}$, while the average gradient in the H-mode was roughly $\nabla V_{pol} \sim 0.5$ (km/s)/cm $\approx 5 \times 10^4\ s^{-1}$. Obviously there are considerable variations about these averages; on the other hand, at some radii in the H-mode the velocity gradient is considerably less than this average. Inside the separatrix the error bars are too large to estimate a gradient for the L-mode cases; however, for at least two of the H-mode cases the gradients inside the separatrix are similar to those outside the separatrix.

The error bars derived from the velocity fits for Fig. 7 were generally smaller in H-mode than in L-mode shots, similar to the trend seen in Fig. 6. In other words, the fluctuations in the poloidal velocity were lower in the H-mode than in the L-mode, at least averaged over 1.2 ms of these images. For example, in the region $(r-r_{sep}) > 0$ the error bars for the H-mode cases was typically ± 0.15 km/s, while for the L-mode cases it was typically ± 0.3 km/s.

In summary, the results from Figs. 6 and 7 indicate that the fluctuations in the poloidal turbulence velocity were lower in the H-mode than in the L-mode, and the average radial gradient of V_{pol} was somewhat smaller in H-mode than L-mode plasmas, at least outside the separatrix. Some uncertainties and limitations of these results are discussed below.

E. Limitations and Uncertainties

There are several significant limitations to the present results: (1) the radial range was limited to about ± 5 cm around the separatrix and the poloidal range to ± 10 cm just above the outer midplane; (2) the dataset was limited to a relatively few ($\sim$20) shots at one specific plasma condition; (3) the L-H transition itself was captured by the imaging system in only a very few ($\sim$5) shots, due to the limited frame capacity of the present camera; and (4) the velocity profiles were mainly obtained outside the separatrix.

The analysis presented here was based only on the two-point space versus time cross-correlation functions, which characterized only the average size and velocity of the turbulence. No attempt was made to determine the two-dimensional (2-D) shape or direction of the turbulence, or to evaluate the non-Gaussian or intermittent structure and/or motion. Since the fluctuation level of the GPI light emission is a nonlinear function of the local density (and electron temperature), the observed reduction in the fluctuation level from the L-mode to the H-mode[9] was not used in this analysis.

The main source of uncertainty in these analyses was the relatively small signal/noise level during H-mode discharges, in which the relative fluctuation level and usable radial range of the GPI signals decreased with respect to the L-mode. This may have resulted in a small underestimate of the radial correlation length derived from H-mode images in Fig. 5. On the other hand, the relatively coarse spacing of the available radial chords may have led to a small overestimate of the radial correlation length in Fig. 4. The similarity of these two results suggests that these errors are relatively small.

An additional source of uncertainty was the occasional presence of coherent or quasicoherent MHD fluctuations in the GPI data. This tends to increase the correlation lengths, since MHD-type fluctuations are globally correlated, and could introduce a component of the fluctuation velocity, which is not characteristic of the edge turbulence. However, in the present dataset the MHD-type fluctuations were generally quite small.

Finally, the location of the separatrix as derived from EFIT has a significant uncertainty, even though it was derived using the best available analysis (in the absence of MSE data). For example, by matching the electron temperature profiles from Thomson scattering at the inboard and outboard midplane, an outer separatrix location 3 cm radially inward from the EFIT separatrix was inferred during the H-mode (for shot #113741 at 0.2 s). The electron temperature at this 3 cm inward-shifted separatrix also better matched the expected separatrix temperature from power balance considerations, i.e., it had $T_e \approx 30-80$ eV compared to the much lower (but quite uncertain) T_e at the EFIT separatrix. This apparent discrepancy between the separatrix location from EFIT and power balance has not yet been resolved in NSTX, but may in general be due either to inaccuracies in the EFIT model or to limitations of the standard power-balance model (e.g., the presence of non-Maxwellian distribution functions).

IV. DISCUSSION

A. Comparison with Alcator C-Mod

A comparison of the main results for L-mode plasmas in NSTX with those derived from a similar GPI diagnostic on an Alcator C-Mod is shown in Table II. The toroidal field and plasma density at the edge are about ten times higher on C-Mod than in NSTX, but the edge electron temperatures in C-Mod are only slightly higher than in NSTX. The radial and poloidal turbulence correlation lengths in the C-Mod are about five to ten times shorter than in NSTX, and the poloidal velocity is about five times lower in the C-Mod than in NSTX. However, the radial velocity in both machines is surprisingly similar, where the radial speeds for NSTX are taken from Ref. 9. Note that most of the GPI data from C-Mod comes from outside the separatrix, since the neutral gas does not penetrate as far in C-Mod as it does in NSTX.

TABLE II. A comparison of NSTX and Alcator C-Mod.

	NSTX	Alcator C-Mod
B_{edge}	2–3 kG	40 kG
n_{edge}	$0.2-2\times10^{19}\text{cm}^{-3}$	$2-20\times10^{19}\ \text{cm}^{-3}$
$T_{e,\text{edge}}$	5–50 eV	20–80 eV
L_{pol}	5–9 cm	0.6–1.0 cm
L_{rad}	2–6 cm	0.7–1.5 cm
V_{pol}	≤5 km/s	≤1 km/s
V_{rad}	≤1-2 km/s	≤1.5 km/s

B. Comparison with previous experiments

As far as we know, there have been no previous measurements comparing the radial correlation length of edge turbulence during the L-mode and H-mode phases of the same discharge (or even in the same device). Previously, Langumir probe measurements in PBX-M showed no significant change in the poloidal k spectrum in the transition from the L to the H-mode,[16] and early measurements on TEXT showed a slight reduction of the radial (and poloidal) correlation length near the radial location of the edge shear layer, but only for Ohmic (i.e., L-mode) plasmas.[17] Therefore the results of Figs. 4 and 5 on the structure of turbulence in NSTX in the L-mode versus the H-mode are not inconsistent with any previous measurements.

There have been several previous experiments that have noted a connection between the poloidal flow shear and the edge turbulence and transport. For example, Langumir probe measurements have shown that the turbulence becomes more Gaussian and less intermittent in the strong velocity shear layer at the edge,[18] and the probability distribution function (pdf) of the radial correlation length of the floating potential fluctuations in the SOL of JET became narrower nearer the shear layer.[19] Experiments on several different types of plasmas have also demonstrated the generation of poloidal flows through turbulent Reynolds stress.[20–23]

Previous results on the correlation between edge shear flow and edge turbulence at the L-H transition are few, but mixed. A test of the connection between the L-H transition and the shear-induced decorrelation of turbulence in PBX-M was inconclusive,[23] but some correlation between the turbulence velocity shear rate and the L-H transition was found for DIII-D.[24] Thus, the present results of Fig. 7 appear to be inconsistent with the result of Ref. 24; however, the shear layer in Ref. 24 was located inside the separatrix, whereas the present results were obtained near or outside the separatrix.

C. Theoretical interpretation of the results

The usual models for edge turbulence[4–8] predict a broad k spectrum with a perpendicular scale length $k_\perp\rho_s\sim0.2$. The correlation lengths of $L_{\text{rad}}(\text{FWHM})\approx4$ cm in NSTX roughly agree with this, as discussed previously.[9] Thus, the decrease in turbulence size scale from NSTX to the C-Mod is most likely due to the higher toroidal field in the C-Mod.

The similarity of the radial turbulence velocity between NSTX and the C-Mod can be understood, at least in part, by the "blob model" of edge turbulence propagation, as described in Ref. 25 and references therein. In this model the speed of isolated structures in the scrapeoff layer is determined largely by the electron temperature and major radius, which are similar for both machines. Details of the application of this model to the NSTX data will be described elsewhere.

The standard $E\times B$ flow shear model of the L-H transition predicts that the radial turbulence correlation length should be lower in the H-mode than in L-mode, and that the velocity shear should be higher in the H-mode than in the L-mode. Neither of these trends were observed in the present results (Figs. 4, 5, and 7). However, there are several caveats to keep in mind concerning the interpretation of this apparent disagreement:

(1) the main shear layer causing the L-H transition may have shifted inward during the H-mode and so may not have been within the region measured, even though this region included the high gradient part of the H-mode pedestal (see Fig. 2), and though the EFIT separatrix moved ≤1 cm at the transition. If so, then the observed changes in the measured region may have been a nonlocal effect of this unobserved internal shear layer,
(2) the measured scale lengths and velocities were averaged over ≈1 ms, so would not have detected faster transient changes in correlation lengths near the L-H transition, or shorter time scale zonal flows or geodesic acoustic modes (GAMs). The only exception was the data from the L-H transition shots in Fig. 7, which did have sub-ms time resolution and did show a slight reduction in L_{rad} from the L-mode to the H-mode,
(3) only the poloidal "group" velocity of the turbulent fluctuations was measured, not the $E\times B$ poloidal flow speed itself; however, a previous experiment suggested that the former was better correlated with the L-H transition in DIII-D,[24]
(4) only the average correlation lengths were evaluated in this analysis and not the k_r spectra, so it may be that the flow shear was affecting only part of k_r spectrum.

Finally, since there is no specific turbulence simulation showing an L-H transition for NSTX, we cannot yet make a quantitative statement concerning the comparison of the results of this experiment with theory. Yet it is interesting to note that the estimated shearing rate of this turbulence during the H-mode of $\tau_s\sim\nabla V_{\text{pol}}(L_{\text{rad}}/L_{\text{pol}})\sim2-3\times10^4\ \text{s}^{-1}$ is close to the inverse of the measured autocorrelation time $\tau_a\approx2\times10^{-5}$ s, i.e., not far from the standard $E\times B$ flow-shear-stabilization criterion.

D. Directions for future work

There are many possible directions for further work in this area. The quality of the data could be improved with higher space and time resolution, and the quantity of the data can be greatly improved with a continuous high-frame-rate camera. The analysis of the data could be significantly improved by evaluating the k spectra, by using higher-order

statistical measures such as the bicoherence spectrum, and by developing algorithms to measure the 2-D velocity fields.[26] Ultimately the most important goal is to quantitatively compare the measurements of turbulence with specific theoretical models. Some promising results in this direction have been obtained,[27–29] but much remains to be done.

E. Conclusions

In this paper we compared the structure and motion of edge turbulence observed near the outer midplane in L-mode vs. H-mode plasmas in NSTX. At the measurement locations, which were near or just outside the magnetic separatrix, there was a qualitative decrease in the turbulence at the L-H transition. However, the radial and poloidal correlation lengths of the turbulence were not significantly different between the L-mode and the H-mode, and the average radial gradient of the poloidal velocity of the turbulence was smaller in the H-mode than in the L-mode plasmas. The most significant change from in the turbulence from the L-mode to the H-mode was a decrease in the fluctuations in the poloidal velocity of the turbulence, as if the flow was more "frozen" in the H-mode.

It is not yet possible to make a quantitative comparison of these results with any specific theoretical calculation for the L-H transition in NSTX. However, a qualitative and preliminary comparison with the standard $E \times B$ flow shear model was made, and several limitations in our ability to quantify this comparison were discussed. Perhaps the most important of these was that the main shear layer causing the L-H transition may have shifted inward during the H-mode, and so may not have been within the region measured. If so, then the observed changes in the measured region at the transition may have been a nonlocal effect of this unobserved internal shear layer.

ACKNOWLEDGMENTS

We thank the NSTX and Alcator C-Mod teams for their support for these experiments and J. Boedo, O. E. Garcia, T. S. Hahm, K. Hallatschek, C. Hidalgo, B. N. Rogers, B. D. Scott, P. W. Terry, G. R. Tynan, and M. V. Umansky for discussions.

This work was supported by USDOE Contract No. DE-AC02-76CHO3073 (PPPL) and USDOE Cooperative Agreement No. DE-FC02-99ER54 512 (MIT).

[1] J. Bleuel, M. Endler, H. Niedermeyer, M. Schubert, and H. Thomsen, New J. Phys. **4**, 38.1 (2002).
[2] G. R. McKee, R. J. Fonck, M. Jakubowski *et al.*, Phys. Plasmas **10**, 1712 (2003).
[3] A. Fredriksen, C. Riccardi, L. Cartegni, and R. Pecseli, Plasma Phys. Controlled Fusion **45**, 721 (2003).
[4] B. D. Scott, Phys. Plasmas **12**, 062 314 (2005).
[5] M. V. Umansky, T. D. Rognlien, and X. Q. Xu, J. Nucl. Mater. **337**, 266 (2005).
[6] O. E. Garcia, N. H. Bian, V. Naulin, A. H. Nielsen, and J. J. Rasmussen, Phys. Plasmas **12**, 090 701(2005).
[7] R. Singh, V. Tangri, P. Kaw, and P. N. Guzdar, Phys. Plasmas **12**, 092 307092307 (2005).
[8] P. Beyer P, S. Benkadda, G. Fuhr-Chaudier G, X. Garbet, P. Ghendrih, and Y. Sarazin, Phys. Rev. Lett. **94**, 105001 (2005).
[9] S. J. Zweben, R. J. Maqueda, D. P. Stotler *et al.*, Nucl. Fusion **44**, 134 (2004).
[10] R. J. Maqueda, G. A. Wurden, D. P. Stotler *et al.*, Rev. Sci. Instrum. **74**, 2020 (2003).
[11] J. L. Terry, S. J. Zweben, K. Hallatschek *et al.*, Phys. Plasmas **10**, 1739 (2003).
[12] O. Grulke, J. L. Terry, B. LaBombard, and S. J. Zweben, Phys. Plasmas **13**, 012306 (2006).
[13] D. P. Stotler, D. A. D'Ippolito, B. LeBlanc, R. J. Maqueda, J. R. Myra, S. A. Sabbagh, and S. J. Zweben, Contrib. Plasma Phys. **44**, 294 (2004).
[14] S. A. Sabbagh, S. M. Kaye, J. Menard *et al.*, Nucl. Fusion **41**, 1601 (2001).
[15] S. J. Zweben, C. E. Bush, R. J. Maqueda, T. Munsat, D. P. Stotler, J. L Lowrance, V. J. Mastrocola, and G. Renda, IEEE Trans. Plasma Sci. **33**, 446 (2005).
[16] G. R. Tynan, L. Schmitz, L. Blush *et al.*, Phys. Plasmas **1**, 3301 (1994).
[17] Ch. P. Ritz, H. Lin, T. L. Rhodes, and A. J. Wootton, Phys. Rev. Lett. **65**, 2543 (1990).
[18] E. Sanchez, C. Hidalgo, D. Lopez-Bruna *et al.*, Phys. Plasmas **7**, 1408 (2000).
[19] B. Goncalves, C. Hidalgo, C. Silva, M. A. Pedrosa, and K. Erents, J. Nucl. Mater. **337-339**, 376 (2005).
[20] Y. H. Xu, C. X. Yu, J. R. Luo, J. S. Mao, B. H. Liu, J. G. Li, B. N. Wan, and Y. X. Wan, Phys. Rev. Lett. **84**, 3867 (2000).
[21] G. R. Tynan, M. J. Burin, C. Holland, G. Antar, N. Crocker, and P. H. Diamond, Phys. Plasmas **11**, 5195 (2001).
[22] N. Vianello, E. Spada, V. Antoni, M. Spolaore, G. Serianni, G. Regnoli, R. Cavazzana, H. Bergsåker, and J. R. Drake, Phys. Rev. Lett. **94**, 135001 (2005).
[23] G. R. Tynan, L. Schmitz, L. Blush *et al.*, Phys. Plasmas **1**, 3301 (1994).
[24] T. N. Carlstrom, R. J. Groebner, C. Fenzi, G. R. McKee, R. A. Moyer, and T. L. Rhodes, Plasma Phys. Controlled Fusion **44**, A333 (2002); T. N. Carlstrom, Fusion Sci. Technol. **48**, 997 (2005).
[25] D. A. Russell, D. A. D'Ippolito, J. R. Myra, W. M. Nevins, and X. Q. Xu, Phys. Rev. Lett. **93**, 265 001265001 (2004).
[26] G. McKee, R. J. Fonck, D. K. Gupta, D. J. Schlossberg, M. W. Shafer, C. Holland, and G. Tynan, Rev. Sci. Instrum. **75**, 3490 (2004).
[27] U. Stroth, F. Greiner, C. Lechte, N. Mahdizadeh, K. Rahbarnia, and M. Ramisch, Phys. Plasmas **11**, 2558 (2004).
[28] E. Sanchez, C. Hidalgo C, B. Goncalves, C. Silva, M. A. Pedrosa, M. Hron, and K. Erents, J. Nucl. Mater. **337**, 296 (2005).
[29] S. H. Müller, A. Fasoli, B. Labit, M. McGrath, O. Pisaturo, G. Plyushchev, M. Podesta, and F. M. Poli, Phys. Plasmas **12**, 090907 (2005).